A MITC–based procedure for the numerical integration of a continuum elastic–plastic theory of through–the–thickness–jacketed shell structures

R. Serpieri[a,*], S. Sessa[b], L. Rosati[b]

[a]*Department of Engineering, University of Sannio, Piazza Roma, 21, 82100, Benevento, Italy*
[b]*Department of Structures for Engineering and Architecture, University of Naples Federico II, Via Claudio, 21, 80124, Napoli, Italy*

Abstract

Through-the-Thickness Jacketing (TTJ) is a technique for repairing and retrofitting shell structures by inducing in the shell core a beneficial confining stress state created by a net of broadly distributed retrofitting links crossing the shell thickness and tying externally applied layers. The paper presents the systematic derivation, the algorithmic implementation and the numerical assessment of a predictor-corrector computational strategy for the integration of a shell FE-model obtained by combining a discrete MITC quadrilateral element with a layered continuum-based generalized shell theory of structures reinforced by TTJ, essentially based upon a Winkler-like idealization of TT reinforcements. This theory of Through-the-Thickness-Jacketed Shells (TTJS) captures the onset of complex triaxial stress states originated by the interaction between core and through-the-thickness reinforcements.

Results of a set of benchmark numerical applications in OpenSees with flat and curved elastic–plastic shell structures are presented in order to assess and illustrate the consistency and the general modelling features of the proposed TTJS-MITC framework endowed with the Drucker-Prager elastic-perfectly-plastic idealization of the nonlinear behavior of the material composing the shell. Numerical results exhibit quadratic convergence of the proposed computational strategy and indicate that the model is able to capture marked strength increments over the in-plane membrane response, albeit these increments are much lower when the shell

*Corresponding author
Email address: rserpier@unisannio.it (R. Serpieri)

Preprint submitted to Computer Methods in Applied Mechanics and Engineering January 9, 2018

response is predominantly of out-of-plane flexural type.

Keywords: TTJ shells, retrofitted shells, confinement, elastic-plastic analysis, seismic retrofit

1. Introduction

Retrofit reinforcement of shell structures is receiving growing attention in the last decades due to the increased importance of repair and rehabilitation in several fields of applied structural engineering such as seismic retrofit [1] and repair of metallic and composite aircraft structures [2].

Continuum-based composite laminated shell theories and finite element interpolations are generally considered to be appealing first-choice tools for the stress analysis of shell structures with in-built or retrofitted reinforcements [3, 4, 5, 6] because of their capability to accurately describe both global and local behaviors of nonlinear structural elements without excessive computational effort [7, 8]. Among more recent trends, basis functions with a high degree of continuity, such as NURBS of isogeometric analysis [9] or mixed shell-solid elements [10, 11, 12], are being increasingly exploited for interpolating mid-plane kinematics [13, 14] as well as for the Through-the-Thickness (TT) kinematics [15], given their ability to achieve an improved representation of stresses and, in particular, accurate descriptions of three-dimensional stress states inside the shell core.

An important application in the repair of shell and frame structures – yet challenging from the modelling point of view – is the enforcement of retrofitted multiaxial confining stress states. In civil engineering the beneficial effect of confinement on ductility and strength of frictional materials is well known (with prestressed concrete being its primary application) and largely employed also in the design of retrofitted devices improving the behavior of masonry [16] and concrete [17] elements. In design practices, account of the interaction between the retrofitted reinforcement and the primary structure object of repair is frequently introduced in the analysis in a simplified uncoupled form by employing increased strength and ductility parameters: for masonry and concrete these are experimentally calibrated [18, 19] over confined columns [20, 21, 22]. This simplified methodology is shortly referred to as Strength Increment-Based (SIB) approach.

On the other hand, more refined continuum-based structural models, inclusive of the kinematic state of the reinforcement, permit to capture important and structurally relevant features of the interaction between reinforced structures and confining devices which cannot be surrogated by simpler uncoupled SIB approaches

[23] The resort to continuum-based shell models is convenient, in particular, for modelling Through-the-Thickness Jacketing (TTJ) in two-dimensional structures [24].

TTJ is a confinement technique exploited in civil engineering for repairing shell structures made of different materials, such as concrete and masonry. Confinement is created by applying broadly distributed retrofitted links crossing the shell thickness and tying externally applied confining layers. For masonry reinforcements, links made of steel and FRP are employed [25, 26, 27] while, among other solutions, textile reinforced plasters are employed for the confining layers [28].

Recent experimental [29] and numerical investigations [30, 24] on planar shear walls have shown that, in order to properly evaluate several structurally-relevant effects of TTJ on the in-plane and out-of-plane responses, there is necessity of fully 3D [23] and 2D [24] structural analyses comprehensively accounting for the interaction of the retrofitting TTJ devices with the whole shell structure.

In particular, a continuum-based generalized laminated shell theory has been proposed in [24] for the triaxial stress analysis of TTJ in laminated composite Shell structures (TTJS), which is by far computationally less expensive than full 3D analyses. The action of the distributed links in TTJS is smeared by a Winkler-like idealization. Such a continuum formulation was found to effectively capture complex triaxial stress states due to the interaction between the shell core and the TT reinforcements. When this framework is combined with Von Mises and Drucker-Prager elasto-plasticity for the constitutive response of the individual laminae, TTJ confinement determines a stress redistribution in the post-elastic phase which results into non-negligible effects of increased stiffness, strength and ductility of retrofitted panels; for instance, modelling concrete as a Drucker-Prager material, strength increase of panels was numerically found to be of 20% approximatively. Notably, these effects were observed not only in the in-plane response, but also in the out-of-plane response, with the latter effect produced, in particular, when an elasto-plastic constitutive behavior with different compressive and tensile strengths, such as Drucker-Prager elasto-plasticity, is employed for the core material.

The present paper presents the systematic derivation, the algorithmic implementation and the numerical assessment of a computational predictor-corrector strategy for the time-integration of a FE-model obtained by combining the TTJS formulation with a discrete MITC quadrilateral [31] shell element. A laminated structure is addressed, with material properties that are piecewise constant across the thickness and layers with elastic-plastic behavior. The algorithmic strategy

solving the nonlinear equilibrium–compatibility problem endowed with arbitratry constitutive models for the individual laminae is reported, together with details on the relevant numerical method implemented in OpenSees [32]. Numerical applications are finally presented illustrating the features of the TTJ response for flat and curved shell structures.

2. Continuum TTJ shell formulation

A layered Through-the-Thickness Jacketed Shell formulation (TTJS) is hereby defined as an enhancement of an Equivalent Single Layer First-order Shear Deformation Theory (ESL-FSDT) [5]. The formulation is constructed on the basis of the essential modeling features and assumptions detailed in the following bullet list.

- The presence of a TT reinforcement net within the shell is considered, consisting of Winkler-like (i.e., smeared over the shell midplane) distributed rod springs (in short, ties). The degree of reinforcement is defined by a midplane scalar field of *TT-reinforcement area ratio*, $\mu_t = \Omega_t/\Omega_c$, where Ω_t is the cross-sectional area of TT by-passing ties and Ω_c the unit core shell midplane area. The strain state of the ties is represented in a smeared form by a scalar field ε_t of longitudinal dilatations of the bars. Examples of a discrete net of ties and the corresponding geometric ratio μ_t are illustrated in Figure 1.

- A layered structure is accounted for, divided into three primary subregions: a central layered *confined core region* subject to a full triaxial stress state, crossed by the (smeared) ties plus two optional inferior (-) and superior (+) *unconfined regions* assumed to be in plane stress conditions (see Figure 1).

- Elongations along the thickness of the ties and of the confined shell core are accounted for; to this end a field u_z of TT displacement along the thickness direction z is added among the kinematic descriptors of the standard Mindlin shell formulation.

- The interaction between TT ties and shell core is described under the following two simple assumptions:

  (i) at ties endpoints, a perfect constraint between the TT z displacement of the ties, u_z^t, and the core displacement, u_z, at the external boundaries

of the confined layers is considered by prescribing a common value of TT displacement, viz.: $u_z = u_z^t$;

(ii) tie-core interaction is absent inside the core layer, so that differential elongations between the (smeared) ties and the shell core are permitted in the remaining part of the rods contained within the interior of the confined region;

- Denoting by $\boldsymbol{\varepsilon}$ the strain tensor and by $\boldsymbol{\eta}$ a generic array of history variables definining, for instance, elastic-plastic or elastic-damage behaviors, a 3D generic inelastic constitutive behavior with internal variables is assumed for each elementary layer, based on the assignment of a free energy function $\Phi\left(\boldsymbol{\varepsilon},\, \boldsymbol{\eta}\right)$ and of appropriate complementary evolution equations for $\boldsymbol{\eta}$; a 1D generic inelastic behavior is similarly considered for the (smeared) ties with an energy function $\Phi_t\left(\varepsilon_t,\, \eta_t\right)$.

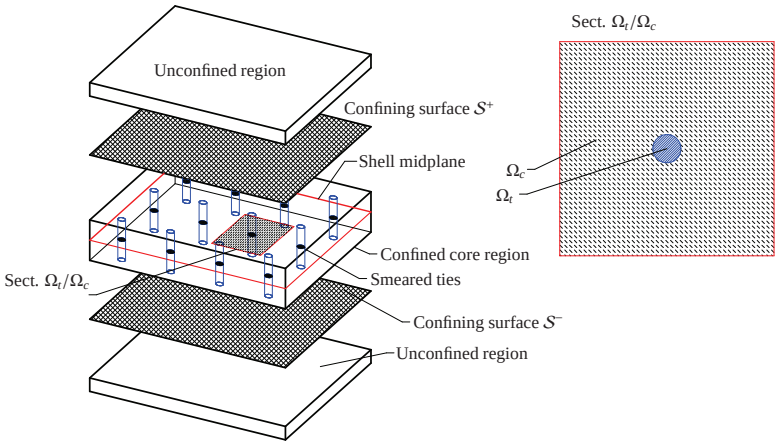

Figure 1: Exploded view of interior confined and exterior unconfined regions of the shell with details of TT reinforcements. $\mathcal{S}^-$ and $\mathcal{S}^-$ are the boundaries of the confined core.

A Cartesian reference frame x, y and z, with associated unit vectors $\hat{\mathbf{x}}$, $\hat{\mathbf{y}}$ and $\hat{\mathbf{z}}$, is considered with origin in the median plane $\mathcal{S}$ of the shell and x and y in-plane axes, see Figure 2. Shell thickness δ is assumed uniform so that exterior surfaces of the shell have coordinates $z = -\delta/2$ and $z = \delta/2$, respectively.

The shell has a laminated structure consisting of N_l layers. As shown in Figure 2, layers are enumerated from bottom to top ($i = 1, \ldots, N_l$), with i_c^- and i_c^+ being the indexes of the lower and upper layers belonging to the confined region.

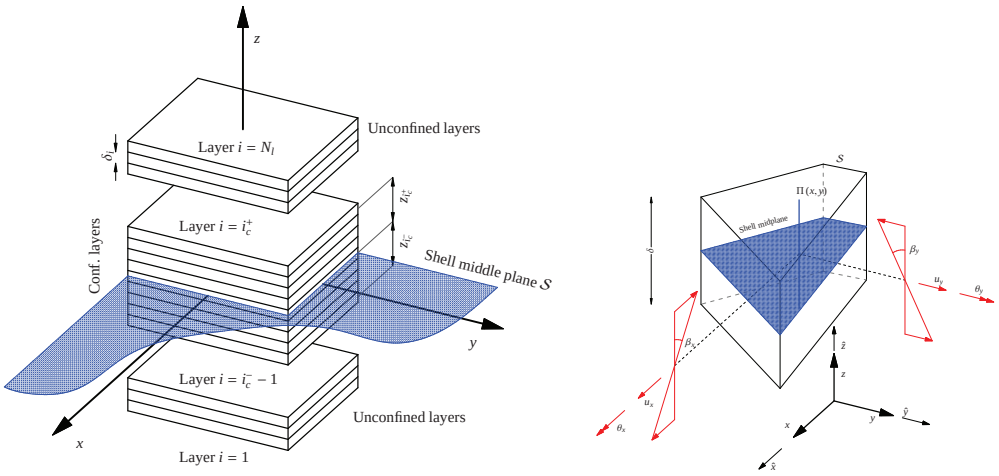

Figure 2: Tripartitioned staking sequence of the shell (left); midplane kinematic descriptors in the ESL-FSDT (right)

As shown in Figure 2, a tripartitioned structure is addressed where the unconfined lower, the internal confined, and the unconfined upper regions correspond to the subsets of indexes $(i = 1, \ldots, i_c^- - 1)$, $(i = i_c^-, \ldots, i_c^+)$, $(i_c^+ + 1, \ldots, N_l)$, respectively, so that the number of confined planes is $i_c^+ - i_c^- + 1$. The thickness of the generic i-th layer and the quota z along the thickness of the midplane of layer i are denoted δ_i and z_i, respectively.

2.1. Kinematics of the TTJ shell

According to the adopted ESL-FSDT kinematics and applying the layer-wise discretization from the outset, displacements $\mathbf{u}$ of the midplane point of the generic i-th lamina, placed at quota z_i, are related to in-plane membrane displacements $\mathbf{u}^{(m)}$ and to generalized plate displacements $\boldsymbol{\beta} = \hat{\mathbf{z}} \times \boldsymbol{\theta}$ (where $\boldsymbol{\theta} = \begin{bmatrix} \theta_x & \theta_y \end{bmatrix}^T$ collects the counter-clockwise rotations about axes x and y) by

$$\mathbf{u}(x,\, y,\, z_i) = \mathbf{u}^{(m)}(x,\, y) + \boldsymbol{\theta}(x,\, y) \times z_i \hat{\mathbf{z}} + u_z\,(z_i)\,\hat{\mathbf{z}}, \qquad i = 1, \ldots, N_l\,. \quad (1)$$

In the previous representation fields $\mathbf{u}^{(m)} = \begin{bmatrix} u_x^{(m)} & u_y^{(m)} \end{bmatrix}^T$, and $\boldsymbol{\beta} = \begin{bmatrix} \beta_x & \beta_y \end{bmatrix}^T$ are defined, as usual, over the median plane $\mathcal{S}$.

As stated, among the basic hypotheses of the model, the employed set of generalized strain measures is enriched by both TT dilatations of the shell core

$\varepsilon_z = \partial u_z/\partial z$ and by longitudinal z strains in the ties, ε_t, that are added to the primary strain descriptors.

Accordingly, the strain state of a given point of the shell midplane is defined by the vector $\boldsymbol{\mathcal{E}}$, collecting Mindlin FSDT generalized shell strains, by the vector $\boldsymbol{\varepsilon}$ collecting TT dilatations, plus the scalar ε_t. The scalar entries of these strain quantities are displayed below altogether:

$$\boldsymbol{\mathcal{E}} = \left[\begin{array}{cccccccc} \mathcal{E}_x^m & \mathcal{E}_y^m & \gamma_{xy}^m & \kappa_x^b & \kappa_y^b & 2\kappa_{xy}^b & \gamma_{xz}^s & \gamma_{yz}^s \end{array} \right]^T, \ \boldsymbol{\varepsilon}_z = \left[\varepsilon_z(z_1), \, \ldots \, , \varepsilon_z(z_{N_l})\right], \ \varepsilon_t \, , \tag{2}$$

where the entries of $\boldsymbol{\mathcal{E}}$ are FSDT membrane $(\mathcal{E}_x^m, \, \mathcal{E}_y^m, \, \gamma_{xy}^m)$, bending $(\kappa_x^b, \, \kappa_y^b, \, \kappa_{xy}^b)$ and shear $(\gamma_{xz}^s, \, \gamma_{yz}^s)$ strain components:

$$\boldsymbol{\mathcal{E}}^m = \text{sym}\left(\mathbf{u}^{(m)} \otimes \nabla_p\right) = \left[\begin{array}{cc} \mathcal{E}_x^m & \gamma_{xy}^m/2 \\ \gamma_{xy}^m/2 & \mathcal{E}_y^m \end{array} \right], \tag{3}$$

$$\boldsymbol{\mathcal{E}}^b = \ \ \text{sym}\left(\boldsymbol{\beta} \otimes \nabla_p\right) = \left[\begin{array}{cc} \kappa_x^b & \dfrac{\kappa_{xy}^b}{2} \\ \dfrac{\kappa_{xy}^b}{2} & -\kappa_y^b \end{array} \right], \tag{4}$$

$$\boldsymbol{\mathcal{E}}^s = \left[\begin{array}{cc} \frac{\partial u_z}{\partial x} + \beta_x & \frac{\partial u_z}{\partial y} - \beta_y \end{array} \right]^T = \left[\begin{array}{cc} \gamma_{xz} & \gamma_{yz} \end{array} \right]^T. \tag{5}$$

A Voigt-like notation for generic 3D second-order infinitesimal strain tensors is adopted to separate strain components associated with the z longitudinal strain moving them to the rightmost position in the array representation. Such a representation reads, for the strain at quota z_i:

$$\boldsymbol{\varepsilon}(z_i) = \left[\begin{array}{c} \boldsymbol{\varepsilon}_0(z_i) \\ \varepsilon_z(z_i) \end{array} \right] = \left[\begin{array}{cccccc} \overbrace{\varepsilon_x(z_i) & \varepsilon_y(z_i) & \gamma_{xy}(z_i) & \gamma_{xz}(z_i) & \gamma_{yz}(z_i)}^{\boldsymbol{\varepsilon}_0(z_i)} & \varepsilon_z(z_i) \end{array} \right]^T. \tag{6}$$

In this way, the enriched ESL FSDT strain state acting in the generic i-th layer (with $1 \leq i \leq N_l$) can be synthetically represented as follows [24]:

$$\boldsymbol{\varepsilon}(z_i) = \mathbb{P}_0(z_i)\boldsymbol{\mathcal{E}} + \varepsilon_z(z_i)\mathbf{P}_z \, . \tag{7}$$

Matrix projectors entering (7) are defined as follows:

$$\mathbb{P}_0\left(z_i\right) = \left[\begin{array}{c} \mathbb{P}^{\star}(z_i) \\ \mathbf{0} \end{array}\right] = \left[\begin{array}{cccccccc} 1 & 0 & 0 & -z_i & 0 & 0 & 0 & 0 \\ 0 & 1 & 0 & 0 & -z_i & 0 & 0 & 0 \\ 0 & 0 & 1 & 0 & 0 & -z_i & 0 & 0 \\ 0 & 0 & 0 & 0 & 0 & 0 & 1 & 0 \\ 0 & 0 & 0 & 0 & 0 & 0 & 0 & 1 \\ \hdashline 0 & 0 & 0 & 0 & 0 & 0 & 0 & 0 \end{array}\right], \qquad \mathbf{P}_z = \left[\begin{array}{cccccc} 0 & 0 & 0 & 0 & 0 & 1 \end{array}\right]^T. \tag{8}$$

In order to simplify some matrix operations reported in the sequel, we denote by $\mathbb{P}^{\star}\left(z_i\right)$ 5×8 the submatrix of $\mathbb{P}_0(z_i)$ obtained by removing the last row in the $\mathbb{P}_0(z_i)$ matrix in (8). This lastly introduced symbol permits to represent $\boldsymbol{\varepsilon}_0$ as $\boldsymbol{\varepsilon}_0\left(z_i\right) = \mathbb{P}^{\star}\left(z_i\right)\boldsymbol{\mathcal{E}}$.

A split completely analogous to (6), is applied to the 3D stress tensors by setting:

$$\boldsymbol{\sigma}\left(z_i\right) = \left[\begin{array}{c} \boldsymbol{\sigma}_0\left(z_i\right) \\ \sigma_z\left(z_i\right) \end{array}\right] = \left[\begin{array}{ccccccc} \overbrace{\sigma_x\left(z_i\right) & \sigma_y\left(z_i\right) & \tau_{xy}\left(z_i\right) & \tau_{xz}\left(z_i\right) & \tau_{yz}\left(z_i\right)}^{\boldsymbol{\sigma}_0(z_i)} & \sigma_z\left(z_i\right) \end{array}\right]^T. \tag{9}$$

As stresses are related to the free energy function by work-association, $\boldsymbol{\sigma} = \partial\Phi/\partial\boldsymbol{\varepsilon}$, the previous split yields the following relation associated with (6):

$$\boldsymbol{\sigma}\left(z_i\right) = \left[\begin{array}{c} \boldsymbol{\sigma}_0\left(z_i\right) \\ \sigma_z\left(z_i\right) \end{array}\right] = \left[\begin{array}{cc} \dfrac{\partial\Phi\left(\boldsymbol{\varepsilon}(z_i),\, \boldsymbol{\eta}_i\right)}{\partial\boldsymbol{\varepsilon}_0\left(z_i\right)} & \dfrac{\partial\Phi\left(\boldsymbol{\varepsilon}(z_i),\, \boldsymbol{\eta}_i\right)}{\partial\varepsilon_z\left(z_i\right)} \end{array}\right]^T, \tag{10}$$

where $\boldsymbol{\eta}_i$ are the i-the layer inelastic history variables.

We further denote by $\boldsymbol{\sigma}$ the generalized stress measures of the shell; their definition naturally stems from the kinematics so far detailed on account of work-association:

$$\boldsymbol{\sigma} = \frac{\partial\Phi^{\Pi}}{\partial\boldsymbol{\mathcal{E}}}, \tag{11}$$

where Φ^{Π} is the energy of the laminated shell chord $\Pi\left(x,\, y\right)$ located at $x,\, y$:

$$\Phi^{\Pi} = \int_{-\delta/2}^{\delta/2} \Phi\left(x,\, y,\, z\right)\, dz. \tag{12}$$

Accordingly, since it trivially turns out to be $\mathbb{P}_0 = \partial\boldsymbol{\varepsilon}/\partial\boldsymbol{\mathcal{E}}$ for the projector in (8), the 8–components stress vector $\boldsymbol{\sigma}$ associated with the generalized strain $\boldsymbol{\mathcal{E}}$, is represented as follows:

$$\boldsymbol{\sigma} = \int_{-\delta/2}^{\delta/2} \frac{\partial \Phi}{\partial \boldsymbol{\varepsilon}}(z)\, \frac{\partial \boldsymbol{\varepsilon}}{\partial \boldsymbol{\mathcal{E}}}(z)\, dz = \int_{-\delta/2}^{\delta/2} (\mathbb{P}_0)^T \boldsymbol{\sigma}\, dz\,. \tag{13}$$

In particular, for the considered layered structures, the components of the generalized shell stress resultants turn out to be:

$$\begin{aligned} \boldsymbol{\sigma} &= \sum_{i=1}^{N_l} (\mathbb{P}_0(z_i))^T \boldsymbol{\sigma}(z_i)\delta_i \\ &= \sum_{i=1}^{N_l} \delta_i \left[\begin{array}{cccccccc} \sigma_x(z_i) & \sigma_y(z_i) & \tau_{xy}(z_i) & -z_i\sigma_x(z_i) & -z_i\sigma_y(z_i) & -z_i\tau_{xy} & \tau_{xz} & \tau_{yz} \end{array}\right]^T \end{aligned}. \tag{14}$$

The stress state of $\Pi(x,\, y)$ is thus completely represented by the arrays $\boldsymbol{\sigma}$ and $\boldsymbol{\sigma}_z = [\sigma_z(z_1),\, \ldots\, , \sigma_z(z_{N_l})]$ plus the scalar σ_t. Observe also that, due to the hypothesis of zero TT normal stress in the unconfined layers, $\boldsymbol{\sigma}_z$ specializes to $\boldsymbol{\sigma}_z = \big[0,\, \ldots\, , 0, \sigma_z(z_{i_c^-}),\, \sigma_z(z_{i_c^-+1}),,\, \ldots\, , \sigma_z(z_{i_c^+}), 0,\, \ldots\, , 0\big]$.

2.2. TTJ equilibrium and compatibility equations

With the employed layered discretization of the shell, the equations describing the perfect constraint between ties and the external boundaries of the confined layers (corresponding to the main assumption (i) stated at the beginning of this section) are written in rate form as follows:

$$\dot{u}_z\left(z_{i_c^-}\right) = \dot{u}_z^t\left(z_{i_c^-}\right), \qquad \dot{u}_z\left(z_{i_c^+}\right) = \dot{u}_z^t\left(z_{i_c^+}\right). \tag{15}$$

Due to the hypothesis of absence of tie-core interaction in the confined region, composed by layers $i = i_c^-,\, \ldots\, ,\, i_c^+$, the (smeared) z longitudinal strain of the ties ε_t will differ, in general, from $\varepsilon_z(z_i)$. A second consequence of this hypothesis is that σ_t is uniform over the length of the smeared tie. Consequently, translational equilibrium in the z direction over a plane parallel to $\mathcal{S}$ and located at quota z_i reads $\Omega_c\sigma_z(z_i) + \Omega_t\sigma_t = 0$. Indicating by $\delta_t = \sum_{i=i_c^-}^{i_c^+} \delta_i$ the total length of the ties, corresponding to the thickness of the confined region, the following equilibrium

and compatibility equations

$$\dot{\sigma}_z\left(z_i\right) + \mu_t \dot{\sigma}_t = 0, \qquad i = i_c^-, \ldots, i_c^+, \tag{16}$$

$$\sum_{i=i_c^-}^{i_c^+} \dot{\varepsilon}_z(z_i)\delta_i = \dot{\varepsilon}_t \delta_t \,. \tag{17}$$

are obtained in time-rate form for the layered discretization at hand.

Denoting as $\mathbb{C}_i$ and C_t the 3D tangent operators of the i-th layer and of the transverse ties at time (or pseudo-time) t, constitutive relationships of the i-layers and of transverse ties are respectively written in rate form as follows:

$$\dot{\boldsymbol{\sigma}}\left(z_i\right) = \mathbb{C}_i \dot{\boldsymbol{\varepsilon}}\left(z_i\right) \tag{18}$$

$$\dot{\sigma}_t = C_t \dot{\varepsilon}_t \,. \tag{19}$$

Note that, for brevity, the actual dependency on history variables of $\mathbb{C}_i$ and C_t has been omitted.

By combining (18) and (7) one obtains:

$$\dot{\boldsymbol{\sigma}}\left(z_i\right) = \mathbb{C}_i \left(\mathbb{P}_0\left(z_i\right) \dot{\boldsymbol{\mathcal{E}}} + \dot{\varepsilon}_z\left(z_i\right) \mathbf{P}_z \right), \qquad i = i_c^-, \ldots, i_c^+ \,. \tag{20}$$

Consistently with the Voigt-like split already used for strains and stresses, we apply to the 6×6 matrices representing the tangent stiffness operators $\mathbb{C}_i$ the following partitioning scheme for a generic stiffness matrix $\mathbb{C}$:

$$\mathbb{C} = \left[\begin{array}{cc} \mathbb{C}^{00} & \mathbf{C}^{0z} \\ \mathbf{C}^{z0} & C^{zz} \end{array} \right] = \left[\begin{array}{ccccc:c} C_{xxxx} & C_{xxyy} & C_{xxxy} & C_{xxxz} & C_{xxyz} & C_{xxzz} \\ C_{yyxx} & C_{yyyy} & C_{yyxy} & C_{yyxz} & C_{yyyz} & C_{yyzz} \\ C_{xyxx} & C_{xyyy} & C_{xyxy} & C_{xyxz} & C_{xyyz} & C_{xyzz} \\ C_{xzxx} & C_{xzyy} & C_{xzxy} & C_{xzxz} & C_{xzyz} & C_{xzzz} \\ C_{yzxx} & C_{yzyy} & C_{yzxy} & C_{yzxz} & C_{yzyz} & C_{yzzz} \\ \hdashline C_{zzxx} & C_{zzyy} & C_{zzxy} & C_{zzxz} & C_{zzyz} & C_{zzzz} \end{array} \right], \tag{21}$$

so that Eqs. (20) become:

$$\dot{\boldsymbol{\sigma}}_0\left(z_i\right) = \mathbb{C}_i^{00}\, \mathbb{P}^{\star}\left(z_i\right)\, \dot{\boldsymbol{\mathcal{E}}} + \dot{\varepsilon}_z\left(z_i\right) \mathbf{C}_i^{0z}, \qquad i = i_c^-, \ldots, i_c^+ \,, \tag{22}$$

$$\dot{\sigma}_z\left(z_i\right) = \mathbf{C}_i^{z0} \cdot \mathbb{P}^{\star}\left(z_i\right)\, \dot{\boldsymbol{\mathcal{E}}} + C_i^{zz} \dot{\varepsilon}_z\left(z_i\right), \qquad i = i_c^-, \ldots, i_c^+ \,. \tag{23}$$

Eqs. (23), combined with (16) and (19) read:

$$C_i^{zz}\dot{\varepsilon}_z\left(z_i\right)+\mu_t C_t\dot{\varepsilon}_t=-\mathbf{C}_i^{z0}\cdot\mathbb{P}^{\star}\left(z_i\right)\,\dot{\boldsymbol{\mathcal{E}}},\qquad i=i_c^-,\,\ldots\,,\,i_c^+\,. \tag{24}$$

Finally, from Eqs. (24) and Eq. (17) a closed system of equations is obtained in the unknowns $\dot{\boldsymbol{\varepsilon}}_z$ and $\dot{\varepsilon}_t$. This system is written below in matrix form:

$$\begin{bmatrix} C_{i_c^-}^{zz} & 0 & \ldots & 0 & \mu_t C_t \\ 0 & C_{i_c^-+1}^{zz} & \ldots & 0 & \mu_t C_t \\ \ldots & \ldots & \ldots & \ldots & \ldots \\ 0 & 0 & \ldots & C_{i_c^+}^{zz} & \mu_t C_t \\ \\ \delta_{i_c^-} & \delta_{i_c^-+1} & \ldots & \delta_{i_c^+} & -\displaystyle\sum_{i=i_c^-}^{i_c^+}\delta_i \\ \\ \end{bmatrix} \begin{bmatrix} \dot{\varepsilon}_z\left(z_{i_c^-}\right) \\ \dot{\varepsilon}_z\left(z_{i_c^-+1}\right) \\ \ldots \\ \dot{\varepsilon}_z\left(z_{i_c^+}\right) \\ \dot{\varepsilon}_t \end{bmatrix} = \begin{bmatrix} -\mathbf{C}_{i_c^-}^{z0}\cdot\mathbb{P}^{\star}\left(z_{i_c^-}\right)\,\dot{\boldsymbol{\mathcal{E}}} \\ -\mathbf{C}_{i_c^-+1}^{z0}\cdot\mathbb{P}^{\star}\left(z_{i_c^-+1}\right)\,\dot{\boldsymbol{\mathcal{E}}} \\ \ldots \\ -\mathbf{C}_{i_c^+}^{z0}\cdot\mathbb{P}^{\star}\left(z_{i_c^+}\right)\,\dot{\boldsymbol{\mathcal{E}}} \\ 0 \end{bmatrix} \tag{25}$$

Solution of system (25) is achieved by first solving equations (24) for $\dot{\varepsilon}_z\left(z_i\right)$, viz.:

$$\dot{\varepsilon}_z\left(z_i\right)=-\frac{1}{C_i^{zz}}\mu_t C_t\dot{\varepsilon}_t-\frac{1}{C_i^{zz}}\mathbf{C}_i^{z0}\cdot\mathbb{P}^{\star}\left(z_i\right)\,\dot{\boldsymbol{\mathcal{E}}},\qquad i=i_c^-,\,\ldots\,,\,i_c^+\,, \tag{26}$$

and by inserting the previous expression into the last equation of system (25) to obtain an equation in the only unknown $\dot{\varepsilon}_t$. To this end, the sum $\sum_{i=i_c^-}^{i_c^+}\delta_i\dot{\varepsilon}_z\left(z_i\right)$ entering this last equation is first computed:

$$\sum_{i=i_c^-}^{i_c^+}\delta_i\dot{\varepsilon}_z\left(z_i\right)=-\left[\sum_{i=i_c^-}^{i_c^+}\delta_i\frac{1}{C_i^{zz}}\mu_t C_t\right]\dot{\varepsilon}_t-\left[\sum_{i=i_c^-}^{i_c^+}\delta_i\frac{1}{C_i^{zz}}\left(\mathbb{P}^{\star}\left(z_i\right)\right)^T\mathbf{C}_i^{z0}\right]\cdot\dot{\boldsymbol{\mathcal{E}}}\,. \tag{27}$$

Substitution of the previous expression into the last equation of system (25) yields

$$-\left[\sum_{i=i_c^-}^{i_c^+}\delta_i\frac{1}{C_i^{zz}}\mu_t C_t\right]\dot{\varepsilon}_t-\left[\sum_{i=i_c^-}^{i_c^+}\delta_i\frac{1}{C_i^{zz}}\left(\mathbb{P}^{\star}\left(z_i\right)\right)^T\mathbf{C}_i^{z0}\right]\cdot\dot{\boldsymbol{\mathcal{E}}}-\sum_{i=i_c^-}^{i_c^+}\delta_i\dot{\varepsilon}_t=0 \tag{28}$$

whose right-hand side contains $\dot{\varepsilon}_t$ as the only unknown. Collection of terms in $\dot{\varepsilon}_t$

provides

$$-\left[\sum_{i=i_c^-}^{i_c^+}\delta_i\frac{1}{C_i^{zz}}\mu_t C_t+\sum_{i=i_c^-}^{i_c^+}\delta_i\right]\dot{\varepsilon}_t-\left[\sum_{i=i_c^-}^{i_c^+}\delta_i\frac{1}{C_i^{zz}}\left(\mathbb{P}^\star\left(z_i\right)\right)^T\mathbf{C}_i^{z0}\right]\cdot\dot{\boldsymbol{\mathcal{E}}}=0\,, \quad (29)$$

so that the rate of the TT strain of the smeared ties can be represented as follows:

$$\dot{\varepsilon}_t=\mathcal{V}\cdot\dot{\boldsymbol{\mathcal{E}}} \quad (30)$$

with

$$\mathcal{V}=-\left[\sum_{i=i_c^-}^{i_c^+}\delta_i\frac{1}{C_i^{zz}}\mu_t C_t+\sum_{i=i_c^-}^{i_c^+}\delta_i\right]^{-1}\left[\sum_{i=i_c^-}^{i_c^+}\delta_i\frac{1}{C_i^{zz}}\left(\mathbb{P}^\star\left(z_i\right)\right)^T\mathbf{C}_i^{z0}\right]\,. \quad (31)$$

Solution of the rate problem is completed by back-substitution of $\dot{\varepsilon}_t$ into the previous equations, through (30). In particular, back-substitution in Equation (26) yields:

$$\dot{\varepsilon}_z\left(z_i\right)=\left[-\frac{1}{C_i^{zz}}\mu_t C_t\mathcal{V}-\frac{1}{C_i^{zz}}\left(\mathbb{P}^\star\left(z_i\right)\right)^T\mathbf{C}_i^{z0}\right]\cdot\dot{\boldsymbol{\mathcal{E}}},\qquad i=i_c^-,\,\ldots\,,\,i_c^+\,. \quad (32)$$

Relations (32) describe the evolution of TT longitudinal strains in compliance with equilibrium and compatibility equations (16) and (17), and in compliance with the constitutive equations of each layer. Consistency with such equations is also kept by the stiffness tangent operator $\mathbb{H}_V$, associated with a generic in-plane point of the shell, that linearizes the relation $\boldsymbol{\mathcal{E}}\rightarrow\boldsymbol{\sigma}$ between generalized shell strains and generalized shell stress resultants

$$\dot{\boldsymbol{\sigma}}=\mathbb{H}_V\,\dot{\boldsymbol{\mathcal{E}}},\qquad \mathbb{H}_V=\left.\frac{\partial\boldsymbol{\sigma}}{\partial\boldsymbol{\mathcal{E}}}\right|_{\overbrace{\boldsymbol{\varepsilon}_z,\;\varepsilon_t}^{rel.}} \quad (33)$$

while $\dot{\boldsymbol{\varepsilon}}_z$ and $\dot{\varepsilon}_t$ keep evolving in compliance with the stated set of TT equilibrium (16), TT compatibility (17) and with the constitutive equations of each layer. We specify that, in order to recall that $\partial\boldsymbol{\sigma}/\partial\boldsymbol{\mathcal{E}}$ is not a partial derivative, yet a derivative computed while $\boldsymbol{\varepsilon}_z$ and ε_t keep the fullfillment of such equations (i.e., while these variables remain *relaxed* over these equations), such compliance is notated in (33) by addition of the subscript $\overbrace{\boldsymbol{\varepsilon}_z,\;\varepsilon_t}^{rel.}$ to $\mathbb{H}_V$. Accordingly, $\mathbb{H}_V$ is computed

from (14)

$$\mathbb{H}_V = \left.\frac{\partial \boldsymbol{\sigma}}{\partial \boldsymbol{\mathcal{E}}}\right|_{\underbrace{\boldsymbol{\varepsilon}_z,\ \varepsilon_t}_{rel.}} = \sum_{i=1}^{N_l} \left(\mathbb{P}_0(z_i)\right)^T \delta_i \left.\frac{\partial \boldsymbol{\sigma}(z_i)}{\partial \boldsymbol{\mathcal{E}}}\right|_{\underbrace{\boldsymbol{\varepsilon}_z,\ \varepsilon_t}_{rel.}} , \tag{34}$$

where the term $\partial \boldsymbol{\sigma}(z_i)/\partial \boldsymbol{\mathcal{E}}|_{\underbrace{\boldsymbol{\varepsilon}_z,\ \varepsilon_t}_{rel.}}$ is provided by the following equation:

$$\dot{\boldsymbol{\sigma}}\left(z_i\right) = \left.\frac{\partial \boldsymbol{\sigma}(z_i)}{\partial \boldsymbol{\mathcal{E}}}\right|_{\underbrace{\boldsymbol{\varepsilon}_z,\ \varepsilon_t}_{rel.}} \dot{\boldsymbol{\mathcal{E}}} = \left[\mathbb{C}_i^{00}\mathbb{P}^{\star}\left(z_i\right) + \frac{\mathbf{C}_i^{0z}}{C_i^{zz}} \otimes \left(-\left(\mathbb{P}^{\star}\left(z_i\right)\right)^T \ \mathbf{C}_i^{0z} + \frac{\mu_t}{\delta_t} C_t \mathcal{V}\right)\right] \ \dot{\boldsymbol{\mathcal{E}}} \tag{35}$$

which is obtained from substitution of (30) into (22). It should be observed that (35) holds for layers of both the confined and of the unconfined regions, where the plane stress condition is recovered by setting for unconfined layers $\mu_t = 0$. This last condition, as it can be checked, recovers the plane stress tangent operator resulting from static condensation over strain ε_z. It can be similarly observed that the limit behavior of zero TT stretch is recovered as $\mu_t \to \infty$. In presence of pure in-plane membrane deformation of the shell, the zero TT stretch condition is equivalent to plane strain.

2.3. Algorithmic implementation

The algorithmic implementation of procedures for integrating the enhanced TTJ shell formulation and for computing the associated algorithmic consistent tangent operator is now described. The algorithm presented herein is based on a recursive procedure to address FE analyses of structures with layers having generic nonlinear constitutive behavior, such as elasto-plasticity and damage models. In this type of analyses the equilibrium-compatibility equation system is strongly nonlinear and closed-form solutions are possible only in simple and very limited cases.

Integration in time (or pseudo-time) of the evolution equations, presented in rate form in the previous subsection, is obtained here employing a full implicit backward-Euler finite time-step scheme. Accordingly, the time interval of the analysis is divided in a finite number of time steps and, for the generic time step $[\theta_n,\ \theta_{n+1}]$, the variables at the initial time instant ($\boldsymbol{\mathcal{E}}^n$, $\boldsymbol{\varepsilon}_z^n$, ε_t^n, $\boldsymbol{\eta}_i^n$ ($i = 1,\ \ldots,\ N_l$), $\boldsymbol{\eta}_t^n$) and the updated shell strain $\boldsymbol{\mathcal{E}}^{n+1}$ are assigned. The problem of determining the updated state variables ($\boldsymbol{\varepsilon}_z^{n+1}$, ε_t^{n+1}, $\boldsymbol{\eta}_i^{n+1}$ ($i = 1,\ \ldots,\ N_l$), $\boldsymbol{\eta}_t^{n+1}$) and the updated FSDT shell stress $\boldsymbol{\sigma}^{n+1}$ of a shell point (typically, a Gauss point belong-

ing to the middle plane of the shell) is solved by enforcing fulfillment of the rate equation at time θ_{n+1} by a predictor-corrector procedure.

To retain generality of the presented scheme, we do not consider any specific constitutive assumption or stacking sequence for the component layers, and we assume that generic time-integration external subroutines are available for each lamina, consistently based on full implicit backward-Euler integration schemes. Given the state variable at the previous time instant $(\boldsymbol{\varepsilon}(z_i)^n, \boldsymbol{\eta}_i^n)$ and the updated strain $\boldsymbol{\varepsilon}(z_i)^{n+1}$, the generic constitutive updating routine of the i-th layer returns the updated stress $\boldsymbol{\sigma}^{n+1}(z_i)$, the updated inelastic variables $\boldsymbol{\eta}_i^{n+1}$, and the consistent algorithmic stiffness tangent operator $\mathbb{C}_i^{n+1}$ at time θ_{n+1}. An algorithm with analogous properties is considered to be available for updating the 1D mechanical state of the smeared ties, viz., given ε_t^n, $\boldsymbol{\eta}_t^n$, and ε_t^{n+1}, the scalars σ_z^{n+1} and C_t^{n+1} are returned.

The algorithm is divided in two nested subroutines. The *outer algorithm* is deputed to handle the tripartitioned unconfined-confined-unconfined sequence of layers and assemble the overall vector of generalized shell stress resultants and the stiffness operator. This routine calls the *inner algorithm* which consists of a Newton-Raphson scheme implementing an iterative predictor-corrector procedure that enforces the finite-step counterparts of the equations of TT equilibrium and compatibility (16) and (17) for the layers in the confined region. In the following, adopting a common convention to display a less dense notation, time subscripts and superscripts $n+1$ are omitted for all trial quantities evaluated at time θ_{n+1}, so that, for instance, a generic variable $\mathbf{q}^{n+1,k}$ is more simply indicated by $\mathbf{q}^k$.

In the implemented Newton-Raphson scheme the trial vector of unknowns related to the generic iteration k is

$$\mathbf{x}^k = \left[\varepsilon_z^k\left(z_{i_c^-}\right),\, \varepsilon_z^k\left(z_{i_c^-+1}\right),\, \ldots,\, \varepsilon_z^k\left(z_{i_c^+}\right),\, \varepsilon_t^k\right]^T = \left[\boldsymbol{\varepsilon}_z^k,\, \varepsilon_t^k\right]^T \tag{36}$$

while the target vector $\boldsymbol{\Psi}$ at iteration k, to be set to zero, contains the residuals of equations (16) and (17), viz.:

$$\boldsymbol{\Psi}_k = \left[\boldsymbol{\Psi}_k^\sigma,\, \Psi_k^\varepsilon\right]^T \tag{37}$$

with

$$\Psi_{k,i}^\sigma = \sigma_z^k(z_i) + \mu\sigma_t^k,\ i = i_c^- \ldots i_c^+, \qquad \Psi_k^{\varepsilon_z} = \sum_{i=i_c^-}^{i_c^+} \varepsilon_z^k(z_i)\delta_i - \varepsilon_t^k\delta_t\,. \tag{38}$$

The recursive instruction in the Newton Raphson scheme is

$$\mathbf{x}^{k+1} = \mathbf{x}^k - \mathbb{J}_k^{-1}\boldsymbol{\Psi}_k \tag{39}$$

with

$$\mathbb{J}_k = \left.\frac{\partial \boldsymbol{\Psi}}{\partial \mathbf{x}}\right|_k . \tag{40}$$

We note in passing that, since rate form equations (16) and (17) can be also written as $\dot{\boldsymbol{\Psi}}\left(\mathbf{x},\, \boldsymbol{\mathcal{E}}\right) = \mathbf{0}$, it follows immediately from the chain derivation rule that

$$\dot{\boldsymbol{\Psi}} = \frac{\partial \boldsymbol{\Psi}}{\partial \mathbf{x}}\dot{\mathbf{x}} + \frac{\partial \boldsymbol{\Psi}}{\partial \boldsymbol{\mathcal{E}}}\dot{\boldsymbol{\mathcal{E}}}\,, \tag{41}$$

so that $\mathbb{J}$ is the square matrix in (25) while $\mathbf{k} = \dfrac{\partial \boldsymbol{\Psi}}{\partial \boldsymbol{\mathcal{E}}}\dot{\boldsymbol{\mathcal{E}}}$ forms the vector of known terms in the same equation. For the computation of $\Delta\mathbf{x}^k = \mathbf{x}^{k+1} - \mathbf{x}^k = \left[\Delta\boldsymbol{\varepsilon}_z^k,\, \Delta\varepsilon_t^k\right] = -\mathbb{J}_k^{-1}\boldsymbol{\Psi}_k$ required in (39) we can consequently take advantage of developments formally analogous to those in (26)–(31) to infer

$$\Delta\varepsilon_t^k = -\left[\sum_{i=i_c^-}^{i_c^+}\delta_i\frac{1}{C_{i,k}^{zz}}\mu_t C_t^k + \sum_{i=i_c^-}^{i_c^+}\delta_i\right]^{-1}\cdot\left[\Psi_k^{\varepsilon} - \sum_{i=i_c^-}^{i_c^+}\delta_i\frac{1}{C_{i,k}^{zz}}\Psi_{k,i}^{\sigma}\right] \tag{42}$$

$$\Delta\varepsilon_z^k\left(z_i\right) = -\frac{1}{C_{i,k}^{zz}}\mu_t C_t^k\Delta\varepsilon_t^k + \frac{1}{C_{i,k}^{zz}}\Psi_{k,i}^{\sigma}, \qquad i = i_c^-,\,\ldots\,,\,i_c^+\,. \tag{43}$$

For the reader's convenience, the outer and the inner algorithms are summarized in Boxes 2.4 and 2.5, respectively. The set of indexes of layers belonging to unconfined region is indicated by $I_u = (1,\,\ldots\,,i_c^- - 1,\,i_c^+ + 1,\ldots\,,N_l)$. Symbol $\mathbb{C}_{pl,i}$ is used in Box 2.4 to indicate the plane-stress tangent operator relevant layer i, with the usual convention of adding of superscripts 00, $0z$, $z0$, zz referring to partitioning of the form in (21). In the norm employed for the convergence criterion in Box 2.5, E_c is a characteristic modulus of the shell core. For greater clarity we remind that time subscripts and superscripts have been omitted for all trial quantities evaluated at time θ_{n+1}.

2.4. Outer algorithm

(i) Read $\boldsymbol{\varepsilon}_0^n$, $\boldsymbol{\varepsilon}_z^n$, ε_t^n, $\boldsymbol{\eta}_i^n$ $(i = 1, \ldots, N_l)$, $\boldsymbol{\eta}_t^n$, $\boldsymbol{\mathcal{E}}$;

(ii) Compute $\boldsymbol{\varepsilon}_0$ strain components at each layer:

$$\boldsymbol{\varepsilon}_0 (z_i) = \mathbb{P}_0 (z_i) \, \boldsymbol{\mathcal{E}}; \quad i = 1, \ldots, N_l \, ;$$

(iii) Get contribution from *confined layers* to the generalized shell stress $\boldsymbol{\sigma}$ and to the tangent operator $\mathbb{H}_V$. To this end, preliminarily solve the nonlinear equilibrium-compatibility problem by calling *Inner algorithm* 2.5 to get:

$$\left(\boldsymbol{\sigma}(z_i), \varepsilon_z(z_i), \mathbb{C}_i, \boldsymbol{\eta}_i, \; i = i_c^- \ldots i_c^+\right) \overset{\text{Inner algorithm 2.5}}{\longleftarrow\!\!-\!\!-\!\!-\!\!-\!\!-} \left(\boldsymbol{\mathcal{E}}, \boldsymbol{\mathcal{E}}^n, \boldsymbol{\varepsilon}^n (z_i) \, , \boldsymbol{\eta}_i^n, \boldsymbol{\varepsilon} (z_i) \, , \; i = i_c^- \ldots i_c^+\right) ; \tag{44}$$

(iv) Get the plane-stress contribution to generalized shell stress and to tangent operator from *unconfined layers*: call external constitutive routines of i-th unconfined layer to get relevant trial updated stress vector $\boldsymbol{\sigma}_0$ and plane-stress tangent operator $\mathbb{C}_{pl,i}$:

$$\boldsymbol{\sigma}_0(z_i), \boldsymbol{\eta}_i, \mathbb{C}_{pl,i}^{00} \overset{\text{plane stress}}{\longleftarrow\!\!-\!\!-\!\!-} \boldsymbol{\varepsilon}_0^n (z_i) \, , \boldsymbol{\eta}_i^n, \qquad i \in I_u \, ;$$

(v) Assemble final updated shell stress resultants:

$$\boldsymbol{\sigma} = \sum_{i=1}^{N_l} \left(\mathbb{P}_0(z_i)\right)^T \boldsymbol{\sigma}(z_i) \delta_i \, ;$$

(vi) Assemble TTJ shell consistent algorithmic tangent operator by using Eqs. (31), (34) and (35):

$$\mathcal{V} = -\left[\sum_{i=i_c^-}^{i_c^+} \delta_i \frac{1}{C_i^{zz}} \mu_t C_t + \sum_{i=i_c^-}^{i_c^+} \delta_i\right]^{-1} \left[\sum_{i=i_c^-}^{i_c^+} \delta_i \frac{1}{C_i^{zz}} \left(\mathbb{P}^\star\left(z_i\right)\right)^T \mathbf{C}_i^{z0}\right];$$

$$\begin{aligned}\mathbb{H}_V \;=\; & \sum_{i=i_c^-}^{i_c^+} \delta_i \left(\mathbb{P}^\star(z_i)\right)^T \left[\mathbb{C}_i^{00}\mathbb{P}^\star\left(z_i\right) + \frac{\mathbf{C}_i^{0z}}{C_i^{zz}} \otimes \left(-\left(\mathbb{P}^\star\left(z_i\right)\right)^T \mathbf{C}_i^{0z} + \frac{\mu_t}{\delta_t} C_t \mathcal{V}\right)\right] \\ & + \sum_{i \in I_u} \delta_i \left[\mathbb{P}^\star\left(z_i\right)\right]^T \mathbb{C}_{pl,i}^{00} \mathbb{P}^\star\left(z_i\right);\end{aligned}$$

(vii) Return.

2.5. Inner algorithm

(i) Get variables $\boldsymbol{\mathcal{E}}$, $\boldsymbol{\mathcal{E}}^n$, $\boldsymbol{\varepsilon}^n\left(z_i\right)$, $\boldsymbol{\eta}_i$, $\boldsymbol{\varepsilon}_0\left(z_i\right)$, $i = i_c^- \ldots i_c^+$ upon calling outer algorithm;

(ii) Set iteration index $k = 1$;

(iii) Initialize $\mathbf{x}^k$ to its converged value of the previous time step:

$$\mathbf{x}^k = \left[\boldsymbol{\varepsilon}_z^k, \varepsilon_t^k\right]^T = \left[\boldsymbol{\varepsilon}_z^n, \varepsilon_t^n\right]^T; \tag{45}$$

(iv) Call constitutive routines of ties and confined layers to get stress values $\boldsymbol{\sigma}^k\left(z_i\right)$ and σ_t^k and the relevant tangent operators C_t^k and $\mathbb{C}_i^k$:

$$\sigma_t^k, C_t^k, \boldsymbol{\eta}_t^k \longleftarrow \varepsilon_t, \boldsymbol{\eta}_t, \varepsilon_t^k,$$

$$\boldsymbol{\sigma}^k\left(z_i\right), \mathbb{C}_i^k, \boldsymbol{\eta}_i^k \longleftarrow \boldsymbol{\varepsilon}_0\left(z_i\right), \varepsilon_z^k\left(z_i\right);$$

(v) Compute residual $\boldsymbol{\Psi}_k = [\boldsymbol{\Psi}_k^{\sigma}, \Psi_k^{\varepsilon}]^T$ by Eqs. (38):

$$\Psi_{k,i}^{\sigma} = \sigma_z^k(z_i) + \mu\sigma_t^k,\ i = i_c^- \ldots i_c^+, \qquad \Psi_k^{\varepsilon z} = \sum_{i=i_c^-}^{i_c^+} \varepsilon_z^k(z_i)\delta_i - \varepsilon_t^k\delta_t\,;$$

(vi) Convergence check of the normalized residual with tolerance λ:

$$\left\| \left[\frac{1}{E_c}\boldsymbol{\Psi}_k^{\sigma} \quad \frac{1}{\delta}\Psi_k^{\varepsilon} \right]^T \right\| \leq \lambda \tag{46}$$

- If Eq. (46) is not fulfilled:
  (a) Update $\mathbf{x}^k$ by Eqs. (42) and (43):

$$\Delta\varepsilon_t^k = -\left[\sum_{i=i_c^-}^{i_c^+} \delta_i \frac{1}{C_i^{zz}}\mu_t C_t + \sum_{i=i_c^-}^{i_c^+}\delta_i\right]^{-1}\left[\Psi_k^{\varepsilon} - \sum_{i=i_c^-}^{i_c^+}\delta_i\frac{1}{C_i^{zz}}\Psi_{k,i}^{\sigma}\right],$$

$$\Delta\varepsilon_z^k(z_i) = -\frac{1}{C_i^{zz}}\mu_t C_t\Delta\varepsilon_t^k + \frac{1}{C_i^{zz}}\Psi_{k,i}^{\sigma}, \qquad i = i_c^-, \ldots, i_c^+,$$

$$\mathbf{x}^{k+1} = \mathbf{x}^k + \left[\Delta\varepsilon_z^k(z_i)\ \Delta\varepsilon_t^k\right]^T;$$

  (b) Set $k = k+1$;
  (c) Go to step iv;
- If Eq.(46) is fulfilled: exit algorithm and return σ_t^k, $\boldsymbol{\sigma}^k(z_i)$, C_t^k, $\mathbb{C}_i^k$, $\boldsymbol{\eta}_t^k$ and $\boldsymbol{\eta}_i^k$.

As shown by the numerical applications illustrated in the next section, the reported algorithm is capable of efficiently computing the triaxial stress-strain state for a variety of constitutive models and geometrical layouts. Clearly, such efficiency remains subordinated to the requirement, typical of Newton-Raphson schemes, that time–steps are not exceedingly large so that the root of the nonlinear algebraic problem solved by the inner algorithm is not too far from the initial trial solution.

A further important requirement to avoid convergence pathologies is that the underlying finite–step problems related to the constitutive updating of component models of layers and of transverse links permain not ill-conditioned. Actually, the inner algorithm exhibits instabilities when strong discontinuities or null eigenvalues in the relevant tangent operators arise in the component constitutive models. In particular, numerical tests have shown instability of the Newton–Raphson algorithm when elastic–perfectly plastic constitutive laws are assumed for the transverse links, within the perfectly plastic plateau regions. In such a case, the residual Jacobian $\mathbb{J}_k$ becomes singular. Conversely, employment of constitutive laws for the transverse links with minimal degrees of convexity and smoothness have proved to ensure stable convergence trends.

3. Numerical applications

The algorithm of Section 2.3 has been implemented in the object–oriented framework for FE analysis OpenSees [32], v.2.5.0, as a new user-defined *ShellSection* class. Such a class, deputed to integrate the complex triaxial stress-strain interaction originated by through-the-thickness jacketing across the layered chords of the shell, is combined with a 4-noded MITC shell element [31, 33] with 6 dofs per node. The tolerance value adopted for all the presented analyses is $\lambda = 10^{-6}$ and, since in all examples the shell material is isotropic, E_c is set to the relevant Young modulus.

Numerical analyses have shown general quadratic convergence of the implemented schemes. Results of a set of analyses related to two selected benchmark examples, described each in a dedicated subsection, are hereby reported to assess and illustrate the consistency and the general modelling features of the TTJS-MITC numerical framework in describing confinement in the response of TTJ-retrofitted shell structures.

Space integration employs a standard Gaussian quadrature with 4 integration points per element while thickness is discretized by 10 layers at each Gauss point. In the reported examples, layers are endowed with elastic-plastic behavior employing J2 or Drucker-Prager yield functions. In particular, J2 examples are included to compare the present results with nonlinear elastic-plastic shell benchmarks retrievable in the literature, which employ Von Mises yield criterion [34]–[35].

A Drucker-Prager yield function [36] is considered in further examples as a simple elastic-plastic description of materials with internal friction. Among several available representations of Drucker-Prager criterion we refer to the represen-

tation of the yield condition [37, 38] $f = J_2 + \rho I_1 - \sqrt{2/3}\sigma_Y \leq 0$, where I_1 and J_2 are, respectively, the first invariant and the second deviatoric invariant of the stress tensor ($I_1 = \mathrm{tr}\,\boldsymbol{\sigma}$, $J_2 = (\mathrm{dev}\boldsymbol{\sigma} \cdot \mathrm{dev}\boldsymbol{\sigma})^{1/2}$, with $\mathrm{dev}\boldsymbol{\sigma} = \boldsymbol{\sigma} - (1/3)I_1\mathbf{1}$, being $\mathbf{1}$ the Voigt vector representing the unit tensor), and where ρ and σ_Y are parameters related to Mohr-Coulomb friction angle ϕ and to cohesion c by:

$$\rho = \frac{2\sqrt{2}\sin\phi}{\sqrt{3}(3-\sin\phi)}, \qquad \sigma_Y = \frac{6c\cos\phi}{\sqrt{2}(3-\sin\phi)}\,. \tag{47}$$

As the entity of confinement is affected by both the area ratio μ_t and the Young modulus E_t of TT ties, the equivalent stiffness parameter

$$k_t = \mu_t E_t \tag{48}$$

is introduced to specify the degree of TT confinement. In the numerical examples this parameter is spanned from the unreinforced plane stress condition, corresponding to the limit of $k_t = 0$, to *zero TT stretch*, recovered when $k_t = \infty$, in order to investigate the sensitivity of the structural response to the full range of conceivable degrees of confinement.

3.1. Dvorkin et al. plastic TT stretching of membrane panel

We first consider the five element patch of an elastic-plastic $10 \times 10\,mm$ square panel subject to in-plane membrane uniaxial stretching, described in [34]. Mesh geometry, with node coordinates, and loading of the panel, having thickness $\delta_t = 1\,mm$, are shown in Fig.3 (left). Elastic properties are those in [34]: linear isotropic elasticity with Young modulus $E = 2.1 \cdot 10^6\,MPa$ and $\nu = 0.3$.

As a preliminary analysis we compare the results concerning a homogeneous panel, considered in [34] by assuming a J2 yield criteron with yield limit $\sigma_Y = 2.1 \cdot 10^3\,MPa$ and isotropic hardening with modulus $E_h = 2.1 \cdot 10^5\,MPa$, with those obtained by the proposed TTJS–MITC formulation in which it has been set $k_t = 0$. TT reinforcement is uniform with respect to the in-plane coordinates, and the confinement condition is enforced to the whole shell thickness, so that no unconfined regions are assumed.

The panel undergoes plastic shrinkage in the TT direction after the yield limit is trespassed. The computed TT stretch is plotted vs. the displacement at the right loaded edge of the panel in Fig. 3 (right) and compared with the corresponding curve computed in [34] by finite-strain analysis with a Von Mises yield criterion therein formulated in terms of Kirchhoff stresses. The curve computed with the

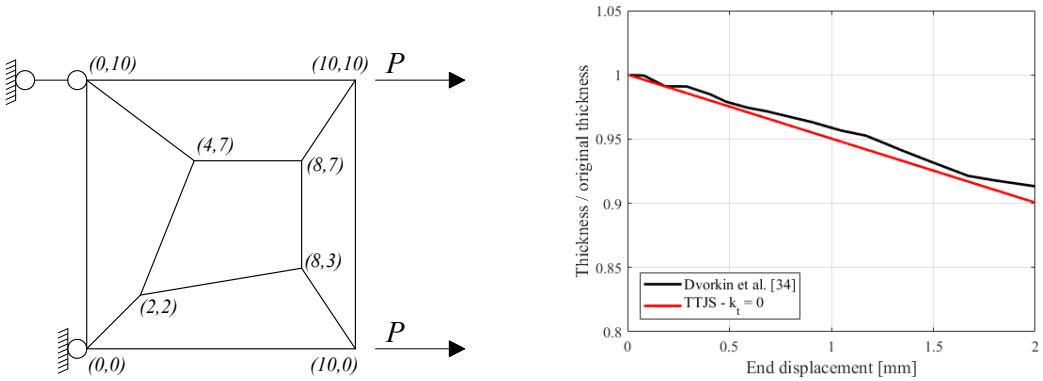

Figure 3: Dvorkin et al. [34]: patch test, geometry (left); thickness ratio vs. end displacement (right)

present framework is linear, and reasonably fits the curve in [34], yet, as expected, with a deviation increasing with the end displacement magnitude. The reason for such a deviation, as well as for the present recovery of a linear curve, is the adoption in the current TTJS-MITC analyses of the linearized kinematics detailed in Section 2.

Table 1 collects the values of the residual norm obtained in a sequence of iterations corresponding to a load step in the elastic-plastic yielding phase. The sequence of residuals is plotted in logaritmic scale as function of the iteration number k in Fig. 4 (solid line). The figure shows that quadratic convergence, corresponding to the ratio $R_k = \|\mathbf{\Psi}_{k+1}\| \,/\, \|\mathbf{\Psi}_k\|^2$ tending to a constant c in the limit $k \to \infty$, is fulfilled. This convergence trend is further highlighted by reporting in the same figure an ideal quadratic sequence fulfilling condition $R_k = c$ at each iteration k. In particular, the reported approximation of the sequence in Table 1 is obtained by setting $\|\mathbf{\Psi}_1\| = 30000$ and $c = 1.864 \cdot 10^{-5}$. Analogous quadratic convergence trends have been observed in the iterations relevant to each Gauss point, element and loading step of the analyses.

Table 1: Residual norm vs. iteration number in a typical iteration sequence within the inner algorithm (taken from the J2 Dvorkin et al. [39] patch test analyses)

Iteration k	Residual norm $\|\Psi_k\|$
1	$9.8 \cdot 10^{-3}$
2	$2.4 \cdot 10^{-3}$
3	$2.2 \cdot 10^{-4}$
4	$1.7 \cdot 10^{-5}$
5	$1.1 \cdot 10^{-10}$
6	$7.7 \cdot 10^{-19}$

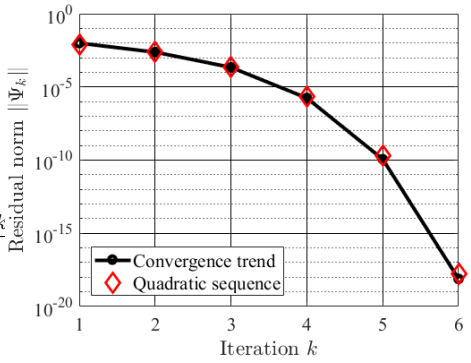

Figure 4: Semilogarithmic plot of residual norm vs. iteration number

The same five-element patch is used for investigating the response of composite TT-reinforced panels. Transverse ties are modeled as linear elastic uniaxial rod elements. As expected, the response of panels endowed with J2 plasticity is found to be not significantly affected by confinement, given the unsensitiveness of J2 criterion to spherical stresses. Conversely, numerical analyses show that use of the Drucker-Prager criterion determines significant strength and stiffness increments. To investigate this effect in presence of a compressive stress state in the panel, a compressive test is considered by reversing the direction of forces P in Fig. 3 (left). Parameters in the Drucker Prager criterion are $\rho = 0.2127$ and $\sigma_Y = 355.176\, MPa$.

Fig. 5 (left) reports the family of end force vs. end displacement curves obtained at different values of k_t and shows that strength and post-elastic stiffness increase with k_t. The corresponding TT stretch vs. end displacement curves, plotted in Fig. 5 (right), consistently show that TT stretch decreases with the degree of confinement.

Figure 6 analyzes the sensitivity to k_t, ν and ρ of the strength increment produced by TT reinforcement, measured as the ratio P_{k_t}/P_u between the strength obtained with a given k_t and the strength P_u of the unreinforced panel at $k_t = 0$. In particular, data shown in the left figure correspond to $\nu = 0.3$ and end displacement $0.1\, mm$ while data in the right figure correspond to $\rho = 0.2127$ and end

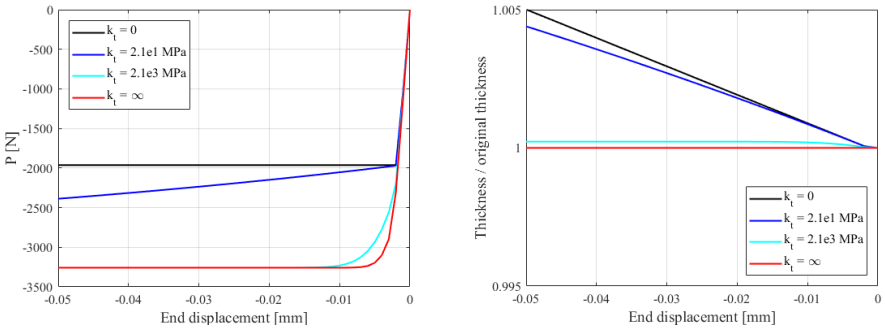

Figure 5: Sensitiviy to TT confinement using a Drucker Prager criterion in Dvorkin et al. [34] uniaxial membrane test with a five element patch: end point load vs. end displacement (left); thickness ratio vs. end displacement (right).

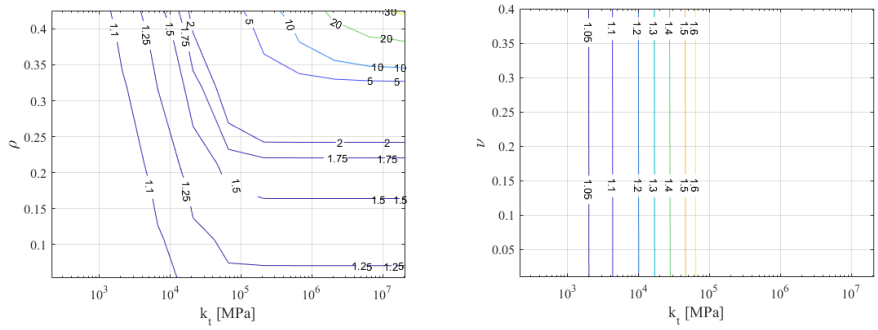

Figure 6: Sensitiviy of strength increment P_{k_t}/P_u to TT confinement using a Drucker Prager criterion in Dvorkin et al. [34] uniaxial membrane test with a five element patch: $\nu = 0.3$, end displacement $0.1\,mm$ (left); $\rho = 0.2127$, end displacement $0.1\,mm$ (right)

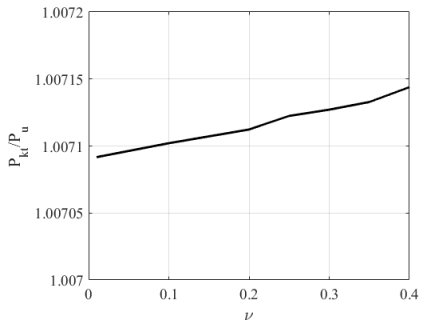

Figure 7: Sensitiviy of strength increment P_{k_t}/P_u to TT confinement using a Drucker Prager criterion in Dvorkin et al. [34] uniaxial membrane test with a five element patch with $\rho = 0.2127$, end displacement $0.1\,mm$ and $k_t = 2700\,MPa$

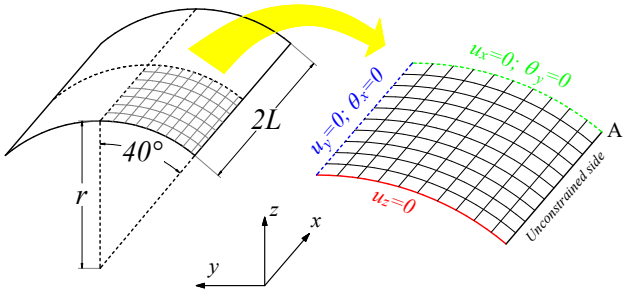

Figure 8: Geometry, constraints and employed mesh for the composite TTJ-reinforced Scordelis–Lo roof

displacement $0.1\,mm$.

For completeness, we specify that the Poisson ratio has a nonzero influence over the panel strength, albeit this is very limited and not apparent from the logaritmic plot of Fig. 6 (right). Figure 7 magnifies this effect by reporting the strength ratio increment P_{k_t}/P_u as function of ν for $k_t = 2700\,MPa$.

3.2. Scordelis–Lo roof

Coupling of membrane and flexural shell responses in presence of TTJ confinement is investigated in a second benchmark which is a composite variant of the Scordelis–Lo roof [40], herein endowed with a varying degree of TT reinforcement.

The geometry and the undeformed mesh are shown in Figure 8. The roof is

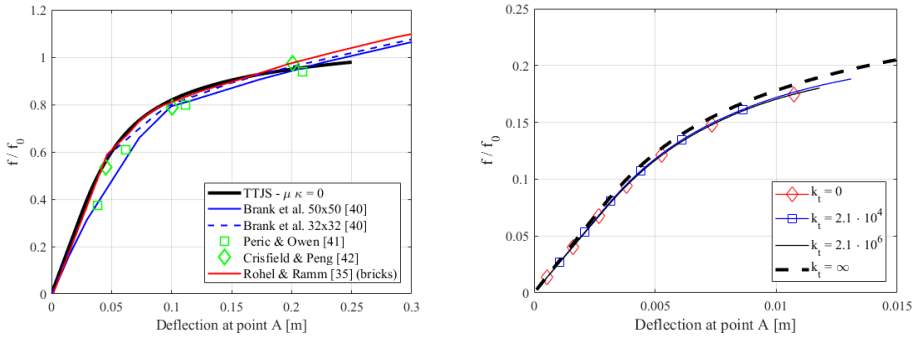

Figure 9: Load – deflection static responses of the Scordelis–Lo roof subject to vertical uniformly distributed load. Comparison with results available in the literature relevant to J2–plasticity constitutive law (left); Responses relevant to the Drucker Prager constitutive model with increasing values of confinement stiffness (right)

a $L = 7.6\,m$ long isotropic barrel vault whose cross section is a circular arch of $40°$, with radius $r = 7.6\,m$ and thickness $\delta = L/100 = 7.6 \cdot 10^{-2}\,m$, pinned along its curved edges and subject to a uniformly distributed vertical self-weight load $f_0 = -4\,kN/m^2$. Young modulus and Poisson ratio are $E = 2.1 \cdot 10^4\,MPa$ and $\nu = 0.0$, respectively. As in the first example, TT reinforcement is uniform, linear elastic and there are no unconfined regions.

On account of the symmetry of geometry and loads, a single quadrant of the roof is analyzed, discretized by a 10×10 mesh (depicted in gray in Fig. 8) and by 10 layers of equal thickness. Use of a more refined mesh yields no appreciable change in the overall structural response.

Quasi-static analyses are performed in displacement control up to a desired maximum displacement. The monitored kinematic parameter, controlling the vertical load $f = \lambda f_0$, is the vertical deflection u at the node corresponding to the middle point of the impost edge (i.e., the right–upper corner of the meshed quadrant shown in Figure 8, where the maximum deflection is attained). For the displacement increment it is set $\delta u = 0.001\,m$.

A first test, in which the constitutive parameters are set to those of the original benchmark of homogeneous roof, has been performed by setting k_t to zero, in order to compare the static response of the implemented formulation with results presented by Brank et al. [41], Peric and Owen [42], Crisfield and Peng [43] and Roehl and Ramm [35] who employed an elastic-perfectly plastic J2 constitutive relationship for the roof material with yield stress $\sigma_Y = 4.2 \cdot 10^3\,MPa$.

Figure 9 (left) presents the load–deflection curves obtained with the J2 Scordelis–Lo roof. The vertical axis reports the ratio f/f_0 while the horizontal axis reports the maximum deflection at the impost edge (point A in Figure 8). Below 0.2 m, the curve matches with those reported in [41]–[35]. The comparison shows a deviation which increases with the maximum deflection, what is explained, similarly to the previous examples, by the employment of linearized kinematics in the present analyses.

To investigate the effects of confinement of structures with internal frictional behavior, a further set of analyses has been performed, also for this second example, by assuming an associative Drucker-Prager elastic-plastic behavior with $\sigma_Y = 0.29\,MPa$ and friction parameter $\rho = 0.2127$. For this second group of analyses, material parameters more closely representative of masonry and concrete, have been used by setting $\nu = 0.3$, and $f_0 = 725.8\,kN$ corresponding to the specific weight per unit volume of tuff masonry ($18\,kN/m^3$). Also in these analyses transverse ties have been modeled as linear elastic.

Figure 9 (right) presents the load–displacement response of the Drucker–Prager Scordelis–Lo roof by sweeping the equivalent stiffness k_t of the transverse ties between zero and infinite. As previously observed in [24] for planar shells, plane stress and zero TT stretch conditions, corresponding to $k_t = 0$ and $k_t = \infty$, represent lower and upper bounds to the structural response of the shell.

The two intermediate values, respectively, $k_t = 2.1 \cdot 10^4\,MPa$ and $k_t = 2.1 \cdot 10^6\,MPa$ have been selected by considering TT steel reinforcements with Young modulus $E_s = 2.1 \cdot 10^5\,MPa$ arranged in equally–spaced square mesh with: diameter $\phi = 8\,mm$ and spacing of about $0.2\,m$ ($k_t = 2.1{\cdot}10^4\,MPa$) and diameter $\phi 12\,mm$ and spacing of approximately $0.1\,m$ ($k_t = 2.1 \cdot 10^6\,MPa$).

The same figure shows that the load-displacement response turns out to be scarcely sensitive to the presence of transverse confinement since curves relevant to $k_t = 2.1{\cdot}10^4$ and $k_t = 2.1{\cdot}10^6$ are almost coincident with the curve corresponding to $k_t = 0$. This trend is in some part expected since, in this structural example, the flexural behavior is predominant with respect to the membrane contribution.

Actually, as shown by a previous research [24], confinement substantially affects the membrane response while its effect on the flexural response is nonzero only when employing yield criteria with different tensile and compressive limits, and mostly negligible compared to the same effect over the membrane response. This trend is confirmed by the colormap in Figure 10 (left) representing the distribution of the transverse stress σ_t for the same structural example, corresponding to $k_t = 2.1 \cdot 10^4\,MPa$.

The confinement stress turns out to be quite limited and negligible in a large

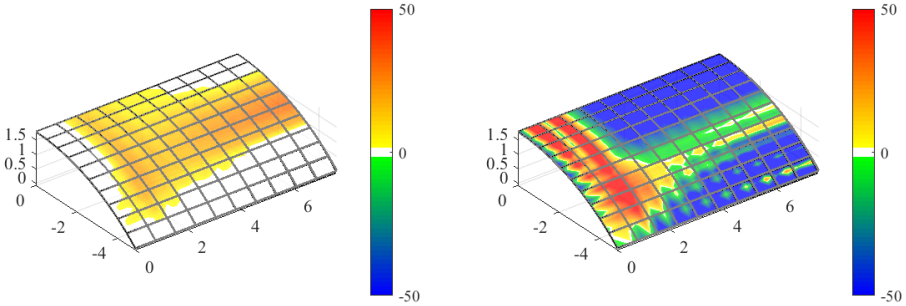

Figure 10: Colormaps of $\sigma_t\,(kPa)$ of the Drucker-Prager Scordelis–Lo roof subject to vertical uniformly distributed load computed with deflection of point A equal to $0.06\,m$ for $k_t = 2.1 \cdot 10^4\,MPa$ (left); and for $k_t = \infty$ (right)

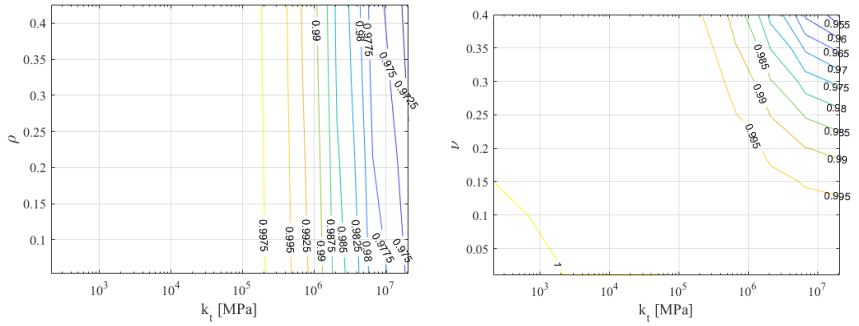

Figure 11: Scordelis–Lo roof – Drucker Prager, Sensitivity: point A displacement ratio $U_{k_t}/U_{k_t=0}$ with $\nu = 0.3$ and load $f = f_0/2$ (left); point A displacement ratio $U_{k_t}/U_{k_t=0}$ with $\rho = 0.2127$ and load $f = f_0/10$ (right)

region of the roof. The relevant upper-bound zero TT-stretch condition is examined in the σ_t colormap of Figure 10 (right). The map shows that, in such a limit situation, the confined region, depicted in red, turns out to be clustered nearby the constrained edge of the roof, while wide regions of the roof domain (depicted in blue) turn out to be subject to negative confinement. Noticeably, the region of the roof at higher σ_t corresponds to the region where the membrane component of deformation prevails over the flexural one, what is consistent with previous observations.

Figure 11 shows the contour plots of the relative deflection as function of k_t, ν and ρ. Relative deflection is measured by the ratio U_{k_t}/U_0 where U_{k_t} is the deflection of point A in Figure 8 attained at a load value $f = f_0/10$ whereas U_0 is the deflection of the same point for the unreinforced roof. Such a ratio is decreasing with k_t thus confirming that stiffness of the structural model increases with k_t. However, such an effect appears to be also in this case rather negligible. Figures 11 (right) and 11 (left) finally show that deflection is decreasing with ν and ρ.

4. Conclusions

A predictor-corrector strategy has been presented for the integration of a laminated FE shell model with retrofitted through-the-thickness confinement, obtained combining a formulation of layered TTJ generalized ESL-FSDT with a four-noded MITC element. A systematic derivation of the related algorithmic implementation and of consistent algorithmic tangent operator has been reported.

Numerical applications have shown quadratic convergence of the implemented schemes, and have confirmed efficiency of this strategy in effectively capturing a complex triaxial interaction between confined shell core and retrofitted reinforment, essentially granted by the adopted simpler 2D shell description. Examples with planar and curved shell structures have permitted to assess the consistency of the response provided by the composite TTJS model against benchmarks of homogeneous elastic-plastic shells considered in the literature.

Examples employing Drucker-Prager yield function have also assessed the overall capability of the MITC-TTJS tool to capture, within the simpler elastic-plastic idealization of the nonlinear behavior of frictional materials, marked strength increments over the in-plane membrane response, albeit much lower when the shell response is predominantly of bending/flexural type.

5. Acknowledgements

This study was funded by Regione Campania and by European funds via the project: “Analisi numerica e prove sperimentali del comportamento di elementi strutturali in calcestruzzo armato soggetti a taglio e flessione composta", Legge 5 Campania - year 2007 (CUP: F82I15000100002).

References

[1] V. M. Karbhari, L. Zhao, Use of composites for 21st century civil infrastructure, Computer Methods in Applied Mechanics and Engineering 185 (2) (2000) 433–454.

[2] C. N. Duong, C. H. Wang, Composite repair: theory and design, Elsevier, 2010.

[3] A. Venkatesh, K. Rao, Analysis of laminated shells with laminated stiffeners using rectangular shell finite elements, Computer Methods in Applied Mechanics and Engineering 38 (3) (1983) 255 – 272.

[4] C.-L. Liao, J. Reddy, Analysis of anisotropic, stiffened composite laminates using a continuum-based shell element, Computers & Structures 34 (6) (1990) 805–815.

[5] J. N. Reddy, Mechanics of Laminated Composite Plates and Shells: Theory and Analysis, Second Edition, 2nd Edition, CRC Press, Taylor & Francis Group, Boca Raton, Fl, USA, 2003.

[6] K. Liew, Z. Lei, J. Yu, L. Zhang, Postbuckling of carbon nanotube-reinforced functionally graded cylindrical panels under axial compression using a meshless approach, Computer Methods in Applied Mechanics and Engineering 268 (2014) 1–17.

[7] N. Valoroso, F. Marmo, S. Sessa, Limit state analysis of reinforced shear walls, Engineering Structures 61 (2014) 127 – 139.

[8] N. Valoroso, F. Marmo, S. Sessa, A novel shell element for nonlinear pushover analysis of reinforced concrete shear walls, Bulletin of Earthquake Engineering 13 (8) (2015) 2367–2388.

[9] J. A. Cottrell, A. Reali, Y. Bazilevs, T. J. Hughes, Isogeometric analysis of structural vibrations, Computer Methods in Applied Mechanics and Engineering 195 (41) (2006) 5257–5296.

[10] D. Magisano, L. Leonetti, G. Garcea, Koiter asymptotic analysis of multilayered composite structures using mixed solid-shell finite elements, Composite Structures 154 (2016) 296–308.

[11] D. Magisano, L. Leonetti, G. Garcea, Advantages of the mixed format in geometrically nonlinear analysis of beams and shells using solid finite elements, International Journal for Numerical Methods in Engineering 109 (9) (2017) 1237–1262.

[12] D. Magisano, L. Leonetti, G. Garcea, How to improve efficiency and robustness of the Newton method in geometrically non-linear structural problem discretized via displacement-based finite elements, Computer Methods in Applied Mechanics and Engineering 313 (2017) 986 – 1005.

[13] J. Kiendl, M. Hsu, M. C. Wu, A. Reali, Isogeometric Kirchhoff-Love shell formulations for general hyperelastic materials, Computer Methods in Applied Mechanics and Engineering 291 (2015) 280 – 303.

[14] D. Benson, Y. Bazilevs, M. Hsu, T. Hughes, Isogeometric shell analysis: The Reissner-Mindlin shell, Computer Methods in Applied Mechanics and Engineering 199 (5) (2010) 276 – 289.

[15] S. Hosseini, J. J. Remmers, C. V. Verhoosel, R. De Borst, An isogeometric continuum shell element for non-linear analysis, Computer Methods in Applied Mechanics and Engineering 271 (2014) 1–22.

[16] A. Borri, G. Castori, M. Corradi, Masonry columns confined by steel fiber composite wraps, Materials 4 (2011) 311–326.

[17] J. C. Teng, J. F. Chen, S. T. Smith, L. Lam, FRP: Strengthened RC Structures, John Wiley & Sons, Inc., Hoboken, NJ, USA, 2001.

[18] M. Corradi, A. Grazini, A. Borri, Confinement of brick masonry columns with CFRP materials, Composites Science and Technology 57 (2007) 1772–1783.

[19] T. Ozbakkaloglu, J. C. Lim, Axial compressive behavior of FRP-confined concrete: Experimental test database and a new design-oriented model, Composites Part B: Engineering 55 (2013) 607 – 634.

[20] J. B. Mander, M. J. N. Priestley, R. Park, Theoretical stress–strain model for confined concrete, Journal of Structural Engineering 114 (8) (1988) 1804–1826.

[21] T. D. Krevaikas, T. C. Triantatillou, Masonry Confinement with Fiber–Reinforced Polymers, Journal of Composite for Construction ASCE 9 (2) (2005) 128–135.

[22] M. Ilyas, S. H. Farooq, A. U. Qazi, R. Umair, Masonry Confinement Using Steel Strips, Pakistan Journal of Engineering & Applied Sciences 5 (2009) 1–9.

[23] X. Liu, T. Medani, A. Scarpas, M. Huurman, A. Molenaar, Experimental and numerical characterization of a membrane material for orthotropic steel deck bridges: Part 2, Finite Elements in Analysis and Design 44 (9-10) (2008) 580 – 594.

[24] S. Sessa, R. Serpieri, L. Rosati, A continuum theory of through-the-thickness jacketed shells for the elasto-plastic analysis of confined composite structures: Theory and numerical assessment, Composites Part B: Engineering 113 (2017) 225 – 242.

[25] M. Valluzzi, F. Da Porto, C. Modena, Behavior and modeling of strengthened three-leaf stone masonry walls, Materials and Structures 37 (3) (2004) 184–192.

[26] D. V. Oliveira, R. A. Silva, E. Garbin, P. B. Lourenço, Strengthening of three-leaf stone masonry walls: an experimental research, Materials and Structures 45 (8) (2012) 1259–1276.

[27] F. F. Pinho, V. J. Lúcio, M. F. Baião, Rubble stone masonry walls strengthened by three-dimensional steel ties and textile-reinforced mortar render under compression and shear loads, International Journal of Architectural Heritage 9 (7) (2015) 844–858.

[28] M. Corradi, A. Borri, G. Castori, R. Sisti, Shear strengthening of wall panels through jacketing with cement mortar reinforced by GFRP grids, Composites Part B: Engineering 64 (2014) 33 – 42.

[29] S. Churilov, E. Dumova-Jovanoska, Analysis of masonry walls strengthened with RC jackets, in: Proc. 15th World Conference on Earthquake Engineering (WCEE), Lisboa, Portugal, 2012, pp. 1–10.

[30] D. Mostofinejad, M. M. Anaei, Effect of confining of boundary elements of slender RC shear wall by FRP composites and stirrups, Engineering Structures 41 (2012) 1 – 13.

[31] K. Bathe, E. N. Dvorkin, Four-node plate bending element based on Mindlin/Reissner plate theory and a mixed interpolation, International Journal for Numerical Methods in Engineering 21 (2) (1985) 367–383.

[32] S. Mazzoni, F. McKenna, M. H. Scott, G. L. Fenves, et al., Opensees command language manual, Pacific Earthquake Engineering Research (PEER) Center.

[33] OpenSees ShellMITC4 element, http://opensees.berkeley.edu/wiki/index.php/Shell_Element, accessed: 2017-07-11.

[34] E. N. Dvorkin, D. Pantuso, E. A. Repetto, A formulation of the MITC4 shell element for finite strain elasto-plastic analysis, Computer Methods in Applied Mechanics and Engineering 125 (1) (1995) 17–40.

[35] D. Roehl, E. Ramm, Large elasto-plastic finite element analysis of solids and shells with the enhanced assumed strain concept, International Journal of Solids and Structures 33 (20) (1996) 3215 – 3237.

[36] D. C. Drucker, W. Prager, Soil mechanics and plastic analysis for limit design, Quarterly of Applied Mathematics 10 (2) (1952) 157–165.

[37] OpenSees Drucker Prager ndMaterial, http://opensees.berkeley.edu/wiki/index.php/Drucker_Prager, accessed: 2017-07-11.

[38] W.-F. Chen, A. F. Saleeb, Constitutive equations for engineering materials: Elasticity and modeling, Vol. 37, Elsevier, 2013.

[39] E. N. Dvorkin, K. J. Bathe, A continuum mechanics based four-node shell element for general non-linear analysis, Engineering Computations 1 (1) (1984) 77–88.

[40] A. C. Scordelis, K. S. Lo, Computer analysis of cylindrical shells, Journal of American Concrete Institute 61 (5) (1964) 539 – 562.

[41] B. Brank, D. Peric, F. B. Damjanic, On large deformations of thin elasto-plastic shells: Implementation of a finite rotation model for quadrilateral shell element, International Journal for Numerical Methods in Engineering 40 (4) (1997) 689–726.

[42] D. Peric, D. R. J. Owen, The morley thin shell finite element for large deformations problems: simplicity versus sophistication, in: Proc. Int. Conf. on Nonlinear Engineering Computations, 1991, pp. 121–142.

[43] M. Crisfield, X. Peng, Efficient non-linear shell formulations with large rotations and plasticity, in: D. R. J. O. et al. (Ed.), Computational Plasticity III: Fundamentals and Applications, Pineridge Press, Swansea, 1992, pp. 1979–1996.